Spatial Encoding In MRI And How To Make It Faster

Polina Golland

May 10, 2000

Abstract

In this report, I review Magnetic Resonance Imaging (MRI) principles and discuss two recently developed techniques for fast MRI. Both methods reduce the imaging time by reducing the number of encoding iterations required for image reconstruction. The first method, SVD MRI, exploits *a priori* knowledge on the signal structure to reduce the number of measurements. The second one, SMASH imaging, uses a partially parallel measurement scheme to recover larger than usual portions of the measurements in every encoding iteration. In addition to the analysis of the methods in the common framework of k-space sampling, their applicability and implementation issues are discussed, error analysis for both methods and the improved reconstruction technique for SMASH imaging are presented.

1 Introduction

Differences in induced magnetization in biological tissues in the presence of a magnetic field are the source of image contrast in MRI. The signal measured by receiver coils is the integral of the induced magnetization over the entire imaged volume, also called the *field of view* (FOV). In order to reconstruct the original 3D distribution of magnetization, a spatially varying field pattern has to be generated in the volume, so that voxels at different locations produce a signal that is "tagged" with the information on the location. Most spatial encoding schemes trade off the quality of the resulting image (spatial resolution and signal-to-noise ratio) against the time of acquisition. While the standard techniques for spatial encoding in MRI produce high quality images, they require a relatively long time to obtain an image (seconds to obtain a 2D image, up to several minutes for a 3D image). The two MRI techniques reviewed in this report, SVD MRI [17, 19] and SMASH [12, 13], are examples of fast MRI, aiming at imaging time reduction without sacrificing too much of the image quality. Each method is represented by an early paper that introduces the algorithm and a later paper that discusses the authors' experience, provides more results, etc.

This report consists of two parts. The first part is a comprehensive overview of MRI principles and relevant imaging techniques. It also contains a discussion on the need for fast MRI, as well as existing methods for increasing the imaging speed. In the second part, the two fast MRI techniques are introduced and discussed. My original contributions consist of the reconstruction error analysis for both methods, as well as a proposed improved reconstruction algorithm based on SMASH technique.

2 MRI Principles

This review is based on several general MRI textbooks [15, 3, 9], as well as on-line sources [7, 16].

2.1 NMR phenomenon

Nuclear magnetic resonance (NMR) is a quantum mechanical phenomenon if considered on the level of single atoms, but classical mechanics can still be used to describe the total magnetization behavior in a volume. This section is based on the classical mechanical interpretation. The quantum mechanical explanation of magnetic resonance (yielding, of course, the same general result) can be found in [7] and [15], pp. 397-399.

Stationary field. Most MRI is based on magnetic resonance in hydrogen nuclei, i.e., single protons. Consider a single proton with angular momentum $\mathbf{I}$ associated with its spin. The dipole magnetic momentum associated with the proton is

$$\boldsymbol{\mu} = \gamma \mathbf{I}, \tag{1}$$

where $\gamma = e/2m$ is *a gyro-magnetic ratio.* If placed in a magnetic field $\mathbf{B}$, the magnetic dipole will experience torque causing change in the angular momentum:

$$\frac{d\mathbf{I}}{dt} = \boldsymbol{\mu} \times \mathbf{B}. \tag{2}$$

Combining Eq. (1) and Eq. (2), we obtain the Larmor equation

$$\frac{d\boldsymbol{\mu}}{dt} = \gamma \boldsymbol{\mu} \times \mathbf{B} \tag{3}$$

that describes precession of $\boldsymbol{\mu}$ around $\mathbf{B}$ with angular velocity

$$\boldsymbol{\omega} = -\gamma \mathbf{B}, \tag{4}$$

also called *Larmor frequency* (Fig. 1a). Note that the magnitude of the dipole magnetic momentum remains the same.

The total magnetic momentum $\mathbf{M}$ of a sample, also called magnetization, is a vector sum of magnetic momenta of individual nuclei. It is easy to show that $\mathbf{M}$ satisfies the Larmor equation (3) as well. In the absence of an external magnetic field, the individual momentum orientation is random over the volume, and the total magnetization is zero. This changes if an external magnetic field $\mathbf{B_0} = B_0\hat{\mathbf{z}}$ is applied to the sample. A small fraction of dipoles (about one in 10^5) aligns with the external field, creating a non-zero magnetization of the sample in the z-direction. Since individual dipoles are out of phase, the *transverse* component M_{xy} of the total magnetization is still zero.

Rf pulses. If a time-varying magnetic field $\mathbf{B}_1$ (a radio frequency (rf) pulse) is applied in the plane perpendicular to $\mathbf{B}_0$,

$$\mathbf{B}_1 = B_1 \cos(\omega_1 t)\hat{\mathbf{x}} + B_1 \sin(\omega_1 t)\hat{\mathbf{y}}. \tag{5}$$

the magnetization vector $\mathbf{M}$ tilts away from the z-axis. Precession of $\mathbf{M}$ as described by the Larmor equation (3) creates a variable electro-magnetic field that induces current in the receiver coil.

The analysis of magnetic momentum $\mathbf{M}$ behavior in the presence of such field $\mathbf{B}_1$ is much simpler in a rotating reference frame. Let's consider a reference frame rotating around the z-axis with angular velocity $\boldsymbol{\omega}$. In this reference frame, the Larmor equation (3) becomes

$$\frac{d\mathbf{M}}{dt} = \gamma \mathbf{M} \times \mathbf{B} - \boldsymbol{\omega} \times \mathbf{M}, \tag{6}$$

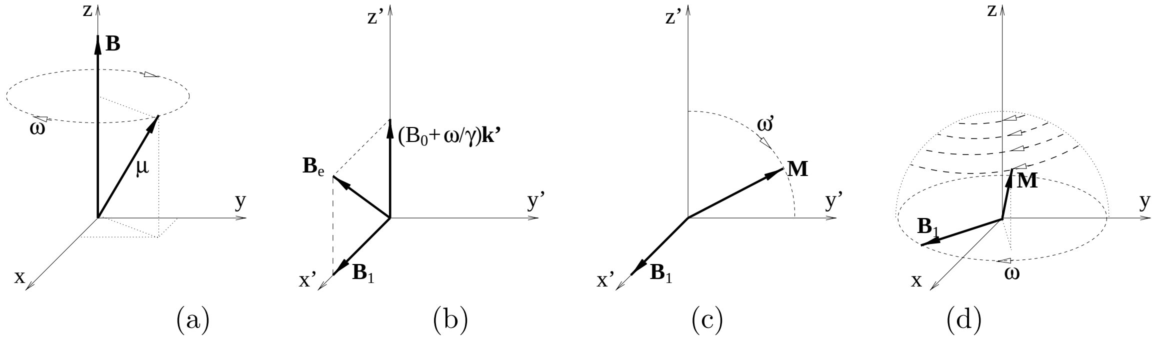

(a) (b) (c) (d)

Figure 1: NMR principles. (a) Larmor precession; (b) Effective magnetic field in the rotating reference frame; (c) Magnetic resonance in the rotating reference frame; (d) Magnetic resonance in the laboratory reference frame.

where the additive term $-\boldsymbol{\omega} \times \mathbf{M}$ represents the difference in motion of $\mathbf{M}$ between the rotating reference frame and the laboratory reference frame. Substituting $\mathbf{B} = \mathbf{B}_1 + \mathbf{B}_0$, we obtain

$$\frac{d\mathbf{M}}{dt} = \gamma \mathbf{M} \times (\mathbf{B}_1 + \mathbf{B}_0 + \boldsymbol{\omega}/\gamma), \tag{7}$$

i.e., in the rotating reference frame, the magnetic momentum $\mathbf{M}$ precesses around the effective magnetic field (Fig. 1b)

$$\mathbf{B}_e = \mathbf{B}_1 + \mathbf{B}_0 + \boldsymbol{\omega}/\gamma = \mathbf{B}_1 + (B_0 + \omega/\gamma)\hat{\mathbf{z}}'. \tag{8}$$

If we choose the reference frame such that $\omega = \omega_1$, then $\mathbf{B}_1 = B_1\hat{\mathbf{x}}'$ and the effective field becomes

$$\mathbf{B}_e = B_1\hat{\mathbf{x}}' + (B_0 + \omega/\gamma)\hat{\mathbf{z}}' \tag{9}$$

(Fig. 1b). Furthermore, if $\boldsymbol{\omega}$ is equal to the Larmor frequency (4), then $\mathbf{B}_e = B_1\mathbf{i}'$ and the motion of vector $\mathbf{M}$ in the rotating reference frame becomes rotation around the x'-axis (Fig. 1c). The amount of this rotation is called the *flip angle*. The angular velocity of that rotation is $\omega' = \gamma B_e = \gamma B_1$. In the laboratory reference frame, $\mathbf{M}$ spirals into xy-plane, as shown in Fig 1d.

If the duration of the rf pulse is τ, the flip angle is

$$\alpha = \omega'\tau = \gamma B_1 \tau, \tag{10}$$

and the transverse magnetization immediately after the pulse is

$$M_{xy} = M \sin\alpha = M \sin(\gamma B_1 \tau), \tag{11}$$

where M is the magnitude of the magnetization $\mathbf{M}$. This transverse magnetization induces current in a receiver coil, producing the signal used in MRI. Flip angles of 90^o are commonly used in MR experiments by setting $\tau = \pi/(2\gamma B_1)$. For such pulses, all of the magnetization is flipped into transverse plane, achieving the strongest possible signal.

Relaxation. Two different types of relaxation are observed in magnetic resonance experiments: longitudinal, or spin-lattice, relaxation and transversal, or spin-spin, relaxation. The effects of relaxation processes are usually negligible during a short rf pulse, but they govern the magnetization behavior in the stationary magnetic field after an rf pulse is switched off.

Spin-lattice relaxation is the process of the total magnetic momentum **M** aligning over time with the stationary magnetic field $\mathbf{B}_0$:

$$M_z = M_0(1 - e^{-t/T_1}), \tag{12}$$

where T_1 is called the *spin-lattice relaxation time*, and M_0 is the equilibrium magnetization that depends on the proton density of the sample and the magnetic field strength B_0. Spin-spin relaxation is due to interactions between spins in the sample. It causes exponential relaxation in the transverse plane:

$$\|M_{xy}\| = M_{xy_0} e^{-t/T_2}, \tag{13}$$

where T_2 is called the *spin-spin relaxation time*, and M_{xy_0} is the transverse magnetization immediately after the rf pulse, which is equal to M_0 for the 90^o rf pulse. Thus, the following equations describe precession of the magnetization vector **M** after a single 90^o rf pulse:

$$\begin{array}{rcl} M_z(t) & = & M_0(1 - e^{-t/T_1}), \\ M_x(t) & = & M_0 e^{-t/T_2} \cos \omega t, \\ M_y(t) & = & M_0 e^{-t/T_2} \sin \omega t, \end{array} \tag{14}$$

where $\omega = \gamma B_0$ is the Larmor frequency. The transverse magnetization is often described as a single complex number:

$$M_{xy}(t) = M_0 e^{-t/T_2} e^{j\omega t}. \tag{15}$$

If a sequence of 90^o rf pulses with a period of T_R (time of repetition) is used, then the longitudinal component of magnetization does not recover to the equilibrium value M_0 and Eq. (15) becomes

$$M_{xy}(t) = M_0(1 - e^{-T_R/T_1}) e^{-t/T_2} e^{j\omega t}. \tag{16}$$

The time between the rf pulse and the time when the signal is measured in the receiver coil, is usually denoted T_E (time to echo). Ignoring the relaxation effects for the duration of the measurement, the transverse magnetization during the measurement is then

$$M_{xy}(t) = M_0(1 - e^{-T_R/T_1}) e^{-T_E/T_2} e^{j\omega t} = \hat{M}_{xy} e^{j\omega t}, \tag{17}$$

where $\hat{M}_{xy} = M_0(1 - e^{-T_R/T_1}) e^{-T_E/T_2}$ is the magnitude of magnetization, and is exactly what MRI attempts to recover. This quantity captures magnetic properties of the material, such as proton density and relaxation times T_1 and T_2. Proton density and relaxation times T_1, T_2 are different for different tissues and are therefore the source of contrast in the images. An excellent discussion on designing pulse sequences, i.e., determining T_R and T_E based on the properties of imaged tissues, can be found in [3], pp. 485-493.

To summarize, magnetization of a sample can be measured by tilting its vector away from the stationary magnetic field. If an rf pulse of Larmor frequency is applied to the sample, magnetic resonance occurs, and the magnetization vector flips into the transverse plane. After the rf pulse is turned off, relaxation processes cause decay of the transverse magnetization and recovery of the longitudinal magnetization component to its original value.

The next section describes how the signal measured by the receiver coil can be used to reconstruct the 3D distribution of $\hat{M}_{xy}$.

2.2 Spatial Encoding in MRI

If a receiver coil is placed along the object, the transverse magnetization induces current in the coil. This signal is the integral of the magnetization over the entire volume:

$$S(t) = \iiint M_{xy}(x,y,z,t)\,dx\,dy\,dz = \iiint \hat{M}_{xy}(x,y,z,t)e^{j(\omega(x,y,z,t)t+\varphi(x,y,z,t))}\,dx\,dy\,dz. \tag{18}$$

The task of spatial encoding is to vary frequency $\omega(x,y,z,t)$ and phase $\varphi(x,y,z,t)$ over the volume for every measurement in such a way that the original distribution of magnetization $\hat{M}_{xy}(x,y,z,t)$ can be recovered from a set of integrals (18). This is achieved by applying a spatially variable (stationary in time) magnetic field $\mathbf{B}'_0(x,y,z) = B'_0(x,y,z)\hat{\mathbf{z}}$ that induces spatial distribution of Larmor frequencies (4) over the volume.

Spatial derivatives of $B'_0(x,y,z)$ determine local resolution of the image. Since constant gradients yield a uniform resolution over the volume, as well as optimal bandwidth characteristics of the current pattern in the gradient coils, linear magnetic fields are commonly used in MRI. In the remainder of this report, we denote the spatially constant derivatives of $B'_0(x,y,z)$ as (G_x, G_y, G_z). Three different types of spatial encoding are commonly used in MRI: selective excitation, phase encoding and frequency encoding.

Selective excitation. If a spatially varying magnetic field $\mathbf{B}'_0$ is followed an rf pulse that contains a selected set of frequencies, magnetic resonance will occur only in a sub-volume whose Larmor frequencies are included in the rf pulse. This technique is commonly used for slice selection in MRI. In this case, $\mathbf{B}'_0 = G_z z\hat{\mathbf{z}}$, and the rf pulse contains a single frequency ω. Only spins in a slice defined by

$$z = \frac{\omega}{\gamma G_z} - \frac{B_0}{G_z} \tag{19}$$

are affected by the rf pulse. It can be shown that the profile of the slice can be approximated by a Fourier transform of the pulse function ([9], pp. 47-52). Thus to select a slice of uniform thickness, sinc rf pulses are used. The signal generated after the pulse is an integration over the selected slice (plane).

Phase encoding. After the excitation pulse, the distribution of transverse magnetization in the sample is essentially 2D. If we apply a linear field of gradient G_y, the Larmor frequency distribution will also be linear in y. This will cause variation in the phase of magnetization. After time τ, the phase of point (x,y) is determined by

$$\varphi(x,y) = (\omega(x,y) - \omega_0)\tau = \gamma G_y y \tau. \tag{20}$$

After the gradient is switched off, the precession frequency returns to a constant value over the plane, while the phase remains proportional to y.

Frequency encoding. If a constant gradient G_x is applied to the sample, the frequency of precession will change linearly with location:

$$\omega(x,y) = \gamma G_x x. \tag{21}$$

If the signal is read off while this gradient is on, contributions of voxels at different locations will have different frequencies.

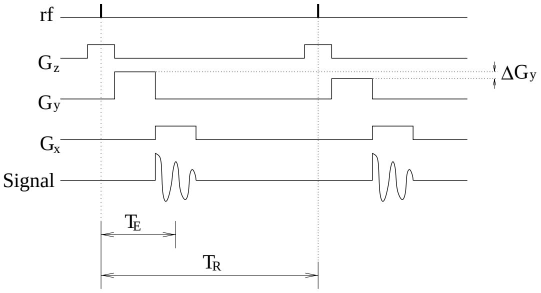

Figure 2: Pulse sequence example for the standard Fourier encoding scheme.

If three encoding steps are performed in a sequence as shown in Fig. 2, at time t after the beginning of the frequency encoding pulse G_x the transverse magnetization of voxel (x, y) in the excited plane is given by

$$M_{xy}(x, y, t) = \hat{M}_{xy}(x, y, t)e^{j(\omega(x,y,t)t+\varphi(x,y,t))} = \hat{M}_{xy}(x, y, t)e^{j(\gamma G_x xt+\gamma G_y y\tau)}, \tag{22}$$

inducing a signal

$$S(t) = \iint M_{xy}(x, y, t)\, dx\, dy = \iint \hat{M}_{xy}(x, y, t)e^{j(\gamma G_x xt+\gamma G_y y\tau)}\, dx\, dy. \tag{23}$$

If we denote

$$k_x = -\gamma G_x t,\ k_y = -\gamma G_y \tau, \tag{24}$$

then

$$S(t) = S(k_x(t), k_y) = \iint \hat{M}_{xy}(x, y, t)e^{-j(k_x x+k_y y)}\, dx\, dy = \mathcal{F}_{\hat{M}}(k_x, k_y), \tag{25}$$

where $\mathcal{F}_{\hat{M}}$ is the Fourier transform of the magnetization at time t. The phase and the frequency encoding steps essentially "tag" every location in the excited slice with a distinct pair of a phase and a frequency of the magnetization precession. The integral of this pattern is the Fourier transform of the magnetization. The signal measured during one such iteration produces a row in the spatial frequency space (k_x, k_y), also referred to as *k-space* in MRI literature. After repeating this process several times for different values of G_y and completing matrix $S(k_x, k_y)$, the image of transverse magnetization can be recovered by applying the inverse discrete Fourier transform. This image is a single slice in the volumetric MRI scan of the sample. To obtain all the slices, the process described above has to be repeated for different values of the excitation frequency ω.

Image quality. Image quality is characterized by its resolution and its signal-to-noise ratio (SNR). Image resolution is determined by the range of acquired frequencies. The Nyquist theorem implies the following inequalities:

$$\Delta x \leq 1/2\Omega_x,\ \mathrm{FOV}_x \leq 1/2\Delta k_x, \tag{26}$$

where Ω_x is the maximal spatial frequency k_x contained in the image, and FOV_x is the size of the image (Fig. 3). Similar inequalities can be obtained for image height (y direction). Traditionally, matrix $S(k_x, k_y)$ is mapped from zero out to higher frequencies k_y. The optimal number of rows/columns measured in k-space is equal to the number of pixels in y/x direction of the image. The optimal spacing in the frequency domain is

$$\Delta k_x^* = 1/2\mathrm{FOV}_x,\ \Delta k_y^* = 1/2\mathrm{FOV}_y. \tag{27}$$

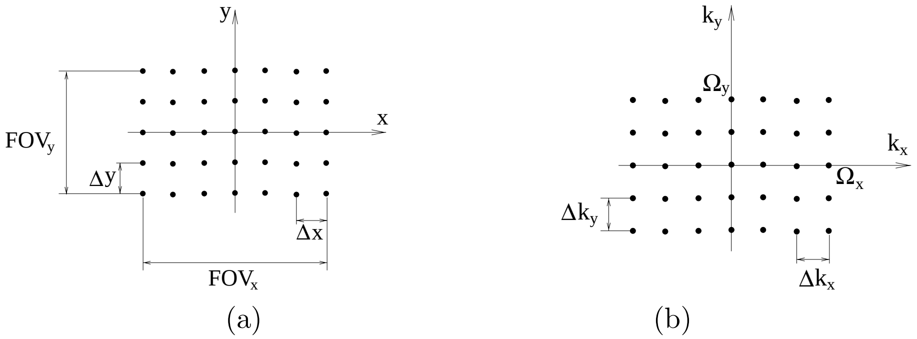

(a) (b)

Figure 3: Spatial encoding. (a) Image domain, (b) k-space.

If the range of frequencies is reduced, the spatial resolution of the image will go down, i.e., the image will look blurred. If the spacing between the measured frequencies is increased, the reconstructed image will suffer from wrapping effects: a smaller FOV determined by Ineq. (26) will be replicated over the image space.

SNR is determined by the amount of measured magnetization relative to thermal noise in the image. Transverse magnetization depends on the power and duration of the rf pulse, as defined by Eq. (11), and on the time interval between excitation pulses T_R (longer T_R allows more of the original magnetization to return to the z-component that can be flipped again in the next cycle). There are several ways to improve SNR of the image: using stronger fields, increasing T_R, averaging over several shots. Many of the parameters are limited by physiological factors, and the current techniques cannot increase the gradient strength or the rf power significantly, as it might cause tissue damage. In addition, acquisition time is limited by motion effects. If a patient moves during imaging, the resulting image will contain artifacts caused by a signal mismatch in consecutive measurements. While motion can be somewhat reduced, it cannot be removed completely in certain applications. Examples include motion due to breathing and cardiac motion. While the former can be eliminated for a short time by a patient holding his breath, the latter hopefully does not stop at any time. Therefore, fast MRI techniques that utilize novel approaches to image encoding to reduce acquisition time, are of great value for medical imaging.

3 Two Fast MRI Techniques

In this part of the report, two different techniques for fast MRI, SVD MRI and SMASH, are reviewed. Both methods modify the standard k-space sampling described in the previous section to reduce the number of encoding steps, thus reducing the total image acquisition time. SVD MRI could potentially improve the imaging time in situations where multiple images of the same patient are acquired during some procedure, but the speedup offered by the technique is limited by the differences between the images. A real time implementation hasn't been demonstrated yet. SMASH is a more mature method that is based on parallel image acquisition using several receiver coils simultaneously. It has been demonstrated in practice with speedup factors up to 6 on cardiac and other images. later in the paper, I propose an improvement to the reconstruction algorithm used by SMASH that will eliminate certain reconstruction errors. For each technique, the details of modified k-space sampling, implementation considerations and experimental results are presented, followed by a discussion of the method.

3.1 SVD MRI

K-space sampling. This method is based on the observation that the Fourier basis, although complete, is not necessarily the optimal basis in terms of the number of encodes, or vectors needed to span the space of rows of $S(k_x, k_y)$. The authors propose using the principal components of the space of image rows for that purpose. Let

$$S = U\Sigma V^T \tag{28}$$

be the singular value decomposition (SVD) of the $N \times N$ matrix S. U and V are orthonormal matrices, and Σ is a diagonal matrix of singular values, ordered in the descending order of their magnitude: $\sigma_1^2 \geq \sigma_2^2 \geq \ldots \geq \sigma_N^2$. In the following derivations, s_k denotes the kth column of matrix S, and s^k denotes the kth row of matrix S.

It is easy to show that the columns of V span the space defined by the rows of S:

$$s^i = \sum_{k=1}^{N} \sigma_k u_k(i) v_k^T, \tag{29}$$

or, in matrix notation,

$$S = \sum_{k=1}^{N} \sigma_k u_k v_k^T. \tag{30}$$

If we want to reduce the number of components $u_k v_k^T$ used to encode S while keeping the sum-of-squares truncation error as small as possible, we have to choose the largest (in magnitude) singular values:

$$\tilde{S} = \sum_{k=1}^{K} \sigma_k u_k v_k^T. \tag{31}$$

Thus an $N \times K$ matrix $\tilde{U}$ of the first K columns of U defines the coefficients of the optimal approximation of S using basis $\{\sigma_k v_k^T\}_{k=1}^{K}$.

The main assumption used by the method is that the magnitude of singular values falls off very quickly for images, and a small number of encodes $\sigma_k v_k^T$ is needed to reconstruct S with very small error. Suppose S is a previously taken image and $S' = U'\Sigma' V'^T$ is the next image. If S' is close to S, then the same encodes should provide a near-optimal reconstruction of S' as well. The algorithm measures $\hat{S}'$ that is effectively equal to $\tilde{U}^T S'$, as explained later in the implementation section. This matrix is then left-multiplied by $\tilde{U}$ to produce the output approximation of S'. If $S' = S$, $\tilde{U}\tilde{U}^T \hat{S}'$ is the optimal approximation of $S' (= S)$ obtained from using the first K singular values. To see that, note that the rows of the measured matrix in this case $\hat{S}' = \tilde{U}^T S' = \tilde{U}^T S$ are exactly equal to $\{\sigma_k v_k^T\}_{k=1}^{K}$.

To summarize, this method measures an approximation of the optimal basis $\{\sigma'_k v'^T_k\}_{k=1}^{K}$ and uses $\{u_k^T\}_{k=1}^{K}$ from the previous image as an approximation of the optimal set of coefficients $\{u'^T_k\}_{k=1}^{K}$ for the reconstruction of S'. The full reconstruction method is actually symmetric, i.e., the result matrix $\hat{S}'$ is an average of the row encoding described above and the column encoding that can be obtained by using columns of U to span the space of columns of S.

In the second paper [19], the authors suggest using several other decompositions that are approximations of SVD that might be preferred in this application for computational reasons. SVD is difficult to parallelize, and real-time dynamic imaging poses time constraints on the processing performed between image acquisitions. Suggested approximations require more encodes to achieve the same precision, but their implementation is better suited for parallel computation.

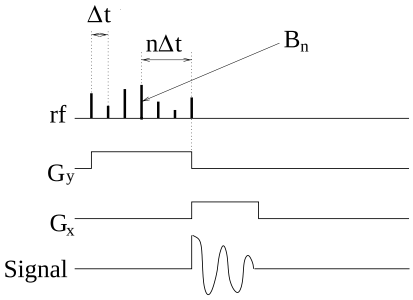

Figure 4: Excitation pulse sequence example for SVD MRI.

Implementation. The phase encoding step of the standard k-space sampling is replaced by an SVD encoding step. The method uses low flip angle (less than 30^o) rf pulses. For small flip angles, Eq. (11) can be approximated by a linear function

$$M_{xy} = M_0 \sin(\gamma B_1 \Delta t) \approx M_0 \gamma B_1 \Delta t. \tag{32}$$

In addition, the longitudinal magnetization after the pulse is non zero:

$$M_z = M_0 \cos(\gamma B_1 \Delta t) \approx M_0. \tag{33}$$

Low flip angle techniques were introduced by Haase *et al.* [5] for fast MRI and have been extensively used in the field. The advantage of this approach is that there is no need to wait for the longitudinal magnetization to recover, as a large amount of magnetization stays parallel to the stationary magnetic field $\mathbf{B}_0$. However, it requires a stronger field to achieve good SNR, as only a small portion of the total magnetization is used for imaging in every iteration.

The encoding is done in iterations. In one iteration, one row of matrix $\hat{S}'$ is computed. To create a spatial distribution of phase, a train of low flip angle rf pulses is used simultaneously with a gradient pulse G_y during the SVD encoding step as shown in Fig. 4. Unlike selective excitation pulses, each rf pulse in the train is wide enough to excite the entire slice plane. The duration of each pulse is Δt, the number of pulses in the train is equal to N. The intensity of pulse n in encoding iteration k is equal to $B_n = u_k(n)$. The time from the end of the pulse n to the end of the gradient pulse is $\tau_n = n\Delta t$. Similarly to the derivation in the previous section, the phase accumulated by the magnetization vector flipped by pulse n is equal to

$$\varphi_n(x, y) = \gamma G_y y \tau_n = \gamma G_y y n \Delta t. \tag{34}$$

Compare to Eq. (20) and (24) to see that if we set

$$G_y = \Delta G_y \tau / \Delta t, \tag{35}$$

where τ is the duration of the standard phase encoding step and ΔG_y is the increment in gradient between two consecutive phase encoding steps, then the accumulated phase is identical to the one in the standard phase encoding step that corresponds to $k_y^n = -\gamma n \Delta G_y \tau$.

The total magnetization after the SVD encoding step is

$$M_{xy}(x, y, t) \quad = \quad \sum_{n=1}^{N} M_{xy}^n(x, y, t) \tag{36}$$

$$\approx \sum_{n=1}^{N} M_z^{n-1}(x,y)e^{-t/T_2}\gamma B_n \Delta t e^{j(\omega(x,y,t)t+\varphi_n(x,y))} \tag{37}$$

$$\approx \sum_{n=1}^{N} M_0(x,y)e^{-t/T_2}\gamma u_k(n) \Delta t e^{j(\omega(x,y,t)t-k_y^n y)} \tag{38}$$

$$= \hat{M}(x,y,t)\sum_{n=1}^{N} u_k(n)e^{j(\omega t-k_y^n y)}, \tag{39}$$

where $\hat{M}(x,y,t) = M_0(x,y)\gamma\Delta t e^{-t/T_2}$ is the magnetization image we want to recover (scaled by a constant $\gamma\Delta t$). Similarly to our derivations in Section 2.2, the resulting signal during the frequency encoding step is

$$\hat{S}'(t) = \iint M_{xy}(x,y,t)\,dx\,dy \tag{40}$$

$$= \iint \hat{M}(x,y,t)\sum_{n=1}^{N} u_k(n)e^{j(\omega(x,y,t)t-k_y^n y)}\,dx\,dy \tag{41}$$

$$= \sum_{n=1}^{N} u_k(n)\iint \hat{M}(x,y,t)e^{-j(k_x(t)x+k_y^n y)}\,dx\,dy \tag{42}$$

$$= \sum_{n=1}^{N} u_k(n)S'(k_x(t),k_y^n), \tag{43}$$

or, in a matrix notation,

$$\hat{s}'^k = u_k^T S', \tag{44}$$

i.e., in a single SVD encoding step, we measure a linear combination of the rows of the original k-space. After K steps, we obtain

$$\hat{S}' = \tilde{U}^T S', \tag{45}$$

which needs to be left-multiplied by $\tilde{U}$ to obtain the near-optimal approximation of S'.

The standard slice selection mechanism cannot be used in conjunction with this technique, as the excitation rf pulses are used for SVD encoding, and cannot be used for slice selection. The first paper [17] proposed to use an additional re-focusing rf pulse for slice selection, but it is not as sharp a selection mechanism as the standard selective excitation step. In fact, this problem was pointer out later by the authors and several methods to fix it were proposed in [10]. The most recent paper on this method [19] still considered only 2D encoding. To the best of my knowledge, no robust 3D encoding scheme with high spatial resolution has been implemented yet.

Experimental Results. Simulations and phantom images were demonstrated in several papers [10, 17, 18, 19]. In these experiments, the reference image was acquired using Fourier encoding, excitation pulse profiles were computed off-line and used for SVD encoding of the next acquired image. While the first paper [17] showed images with wrapping artifacts, one of the later papers [10] demonstrated images with no visible artifacts. The group is currently working on hardware implementation of the method that will enable its testing in a real-time situation, as well as extending this approach into 3D.

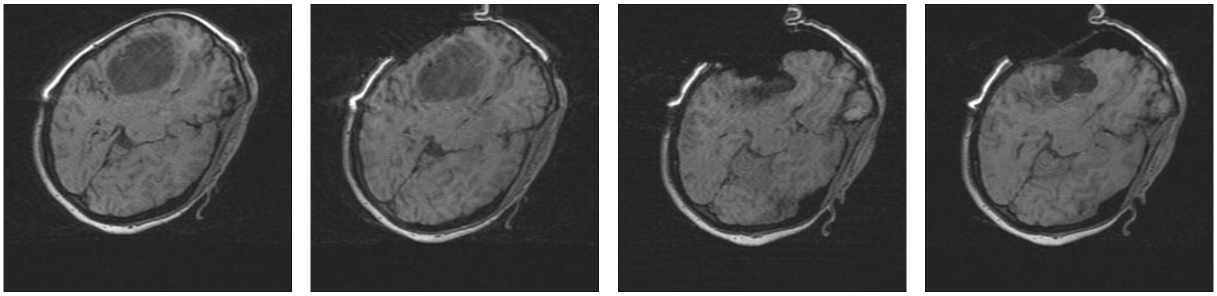

Figure 5: Four images used in the experiments to quantify the relationship between the number of encodes used for imaging and the reconstruction error.

Discussion. The speedup offered by this technique is inversely proportional to the number of encodes used for image acquisition. On the other hand, the reconstruction error increases monotonically as the number of encodes goes down. This section contains a discussion on the authors' analysis of errors and the tests I performed on example brain MRI images to study the trade-off between the error and the speedup.

The two types of errors in the presented technique, a truncation error and a projection error, are caused by different factors and will be considered separately. The truncation error is caused by using only a few principal components to encode the information about the estimated image S. If $S' = S$, the reconstruction error is equal to the truncation error

$$\bar{e}_t(K) = \sqrt{\frac{1}{N^2}\sum_i \sum_j (S(i,j) - \tilde{S}(i,j))^2} = \frac{1}{N}\sqrt{\sum_{k=K+1}^{N} \sigma_k^2}. \tag{46}$$

The authors reference extensive empirical evidence of fast convergence of the truncation error from the field of image processing. However, the nature of the analysis commonly done in computer vision and image processing using SVD is different from the presented technique. Typically, the whole image is considered as a vector, and SVD is used to find principal components that span the space of example images (many examples are usually available at this stage). Then the K largest principal components are selected to reduce dimensionality of the representation. In this case, truncation error $\bar{e}_t(K)$ represents the error of representation of the image examples using the selected principal components. In fact, Cao and Levin [1] proposed using this approach for MRI. They used information on the principal components of the medical image database to reduce the number of phase encoding steps in the standard Fourier encoding. They did not modify the image encoding scheme, but only tried to select "principal frequencies" from the Fourier basis.

In contrast, SVD MRI computes principal components of the space of the rows of S and uses a subset of those for representing the rows. Truncation error $\bar{e}_t(K)$ is computed for a *single* image. While there is strong empirical evidence that natural images span a much lower dimensional space than their number of pixels (N^2 dimensional space), this does not immediately imply that the same is true about rows of a single image matrix (N dimensional space). One can argue that this is true for any slowly varying function, but the quantitative analysis of the rate of convergence is crucial in my opinion. It determines the relationship between the number of encodes, the error of reconstruction and the speedup obtained as a result of applying this technique to MRI.

For this purpose, I ran experiments on several brain images, performing SVD and checking truncation error for different numbers K of encodes. Fig. 5 shows four images used in this test. They were obtained in the open magnet MRI system at Brigham and Women's Hospital, Boston.

The four images are of the same patient obtained during a tumor removal operation. These images simulate the proposed application for SVD MRI fairly well. Fig. 6a shows average truncation error $\bar{e}_t$ as a function of the number of principal components used for the image encoding for these four images. The graphs are in log-scale. We can see that the relationship between the number of significant bits lost in encoding and the number of encodes is almost linear.

The second type of error is what the authors call a projection error. If S' is different from S (which is a more interesting and practical case), the use of $\{v_k\}_{k=1}^K$ as an approximation of $\{v'_k\}_{k=1}^K$ introduces additional error into the reconstruction:

$$\bar{e}(K) = \frac{1}{N}\sqrt{\sum_i \sum_j (S'(i,j) - [\tilde{U}\tilde{U}'S'](i,j))^2}. \tag{47}$$

This is related to a question extensively studied in linear algebra: how well can a linear subspace basis represent vectors from another linear subspace? In [18], the authors proposed studying a distribution of the sines of the principal angles between the two images to answer this question. The nth principal angle is defined as the smallest angle between the nth basis vector in the first subspace and any vector in the second subspace that is orthogonal the $n-1$ previously selected vectors. The sine of a principal angle determines the length of projection error for the corresponding basis vector. Distribution of the sines of the principal angles between two subspaces is used in linear algebra as a measure of similarity between two bases [4].

In [18], the authors empirically tested the technique in several simulated scenarios, using different estimated images S for reconstruction of the same real image S' and varying the number of encodes used for the reconstruction. The estimated images S used in the experiments ranged from a slice in the same scan to white noise. The experiments demonstrated that as the number of encodes increases, a fair quality reconstruction can be achieved. The sine distributions of principal angles were constructed for these different scenarios as well. Similarly to the truncation error analysis, my main concern is the tradeoff between the reconstruction error and the speedup. While [18] contains a lot of qualitative data, it does not provide a quantitative analysis of this tradeoff. Fig 6b shows six graphs obtained by using a different pair of images for every graph as S and S' (the order between the images was preserved, i.e., the images used as S proceeded S'). The graphs demonstrate that actually the subspaces formed by the image rows vary quite a bit between any two different images. To get a mean square error of less than 8 (loosing 3 out of 8 significant bits), one would have to use approximately half of the encodes.

Cao and Levin published a critique of SVD MRI [2], claiming that no new objects will be captured by this technique, especially if the changes correspond to the spatial frequencies not contained in the original image. This claim is not entirely valid, as the principal component basis can represent the entire sub-space, rather than a single image, and for medical images specifically, the changes tend to occur at the boundaries of the objects, corresponding to spatial frequencies contained in the original image. However, this paper raised a point of a similar nature to the questions discussed above, namely, how well can the K largest principal components of one image represent a new image? The space of the image rows is of such high dimensionality that even if the images are perceptually close, their SVD bases can be significantly different. The test results on the brain images shown in Fig 6b demonstrate this point clearly. One cannot expect a speedup of more than 2 if fair quality images are desired. Similar tests have to be run for every type of image before an optimal tradeoff between the reconstruction error and the speedup is determined. Studying the statistics of the distribution from more than one image can help to capture the principal components of the space better. Encodes derived from a set of images would be more stable than the ones derived from a single image. Ideally, SVD MRI and the technique proposed by

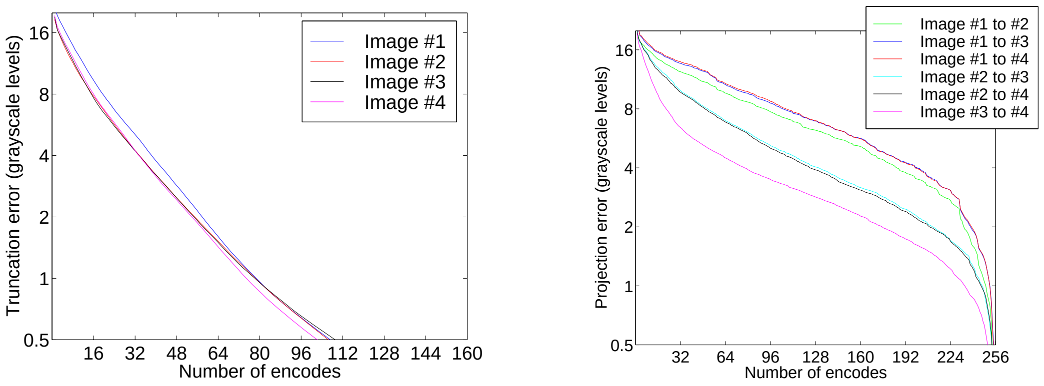

(a) (b)

Figure 6: Reconstruction error. All graphs show an average sum-squares reconstruction error (log-scale) as a function of the number of encodes used. The data is 8bit (256 grayscale levels). (a) Truncation error $\bar{e}_t$, $S' = S$. (b) Reconstruction error $\bar{e}$, $S' \neq S$.

Cao and Levin [1] should be combined to yield a significant improvement over the standard MRI methods. The principal components of the space are to be derived based on more than one image, and then used as a basis for encoding of the next image as proposed by the authors of SVD MRI.

3.2 SMASH Imaging

Most conventional MRI techniques assume that the spatial sensitivity of the receiving coil is uniform over the entire FOV. In fact, a lot of effort goes into making such coils. Parallel imaging techniques exploit spatially varying coil sensitivity to create the encoding pattern. Taking into account the spatial distribution of the coil sensitivity $C(x, y, z)$, Eq. (18) becomes

$$\begin{aligned} S(t) &= \iiint M_{xy}(x, y, z, t) C(x, y, z)\, dx\, dy\, dz \\ &= \iiint \hat{M}_{xy}(x, y, z, t) C(x, y, z) e^{j(\omega(x,y,z,t)t + \varphi(x,y,z,t))}\, dx\, dy\, dz, \end{aligned} \tag{48}$$

and similarly to Eq. (25), for standard Fourier encoding schemes

$$S(t) = \iint \hat{M}_{xy}(x, y, t) C(x, y) e^{-j(k_x x + k_y y)}\, dx\, dy. \tag{49}$$

Using K receiver coils with different sensitivity distributions yields K integrals of the magnetization with different spatial patterns superimposed on the volume in one phase encoding step. This could potentially lead to reduced imaging time or higher SNR, depending on how the measurements from the receiver coils are combined together.

While many parallel techniques have been proposed over the years, most of them have not been implemented in practice. SMASH is the first parallel technique that was demonstrated on real images. SMASH modifies the phase encoding step of the standard Fourier encoding scheme to sample several rows of k-space in a single iteration. Since this is done after the slice excitation step, the analysis in the remainder of this section is essentially 2D.

K-space sampling. Let's consider a coil whose sensitivity $C(x, y)$ is a harmonic function of the phase encoded coordinate:

$$C_m(x, y) = e^{jm\Delta k_y y}, \tag{50}$$

where m is the order of the harmonic, and Δk_y is the spacing between the rows in k-space (Fig. 3b). In the phase encoding step that corresponds to row k_y in k-space, such a coil will receive signal

$$\begin{aligned}\hat{S}(t) &= \iint M_{xy}(x,y,t)C_m(x,y)\,dx\,dy \\ &= \iint \hat{M}_{xy}(x,y,t)e^{jm\Delta k_y y}e^{-j(k_x x+k_y y)}\,dx\,dy \\ &= \iint \hat{M}_{xy}(x,y,t)e^{-j(k_x x+(k_y-m\Delta k_y)y)}\,dx\,dy = S(k_x,k_y-m\Delta k_y),\end{aligned} \tag{51}$$

is equal exactly to a line in k-space that is m lines away from the originally "targeted" line k_y. If we had M coils with sensitivity functions defined by Eq. (50) ($m = 0, \pm 1, \pm 2, \ldots$), we could measure M rows of k-space in a single phase-encoding step, achieving a speedup of M over the standard imaging techniques. This process is illustrated in Fig. 7a.

Coil Sensitivity. Coil sensitivity is usually far from being a harmonic function. More often, a Gaussian function is a better approximation for the coil sensitivity (Fig. 7b). The authors use the least squares fit to approximate each harmonic as a linear combination of the real sensitivity functions $\{D_k(x,y)\}_{k=1}^{K}$:

$$\tilde{C}_m(x,y) = \sum_{k=1}^{K} a_k^m D_k(x,y). \tag{52}$$

Eq. (49), which describes the signal formation process, is linear in the coil sensitivity function. Therefore the images that would have been measured by the virtual coils with sensitivities $\{\tilde{C}_m\}_{m=1}^{M}$ are linear combinations of the images measured by the real coils with weights a_k^m. These "virtual coils" can be combined according to Eq. (51) to reconstruct S.

To measure coil sensitivity functions, the authors originally used phantoms of uniform density. The image of a uniform density phantom is equal to the Fourier transform of the sensitivity function, as can be seen from Eq. (49). In addition to phantoms, the authors suggest using real images in areas of relatively uniform proton density (e.g., spine) to calibrate the system. The advantage of using real images is that the calibration is performed under conditions that are much closer to the coil array configuration during image acquisition, and therefore the estimates approximate the real sensitivity function more accurately.

To summarize, SMASH imaging consists of three steps. First, K coil sensitivity functions $\{D_k(x,y)\}_{k=1}^{K}$ are estimated from phantom images or images of biological tissue of relatively uniform proton density. Then these functions are used to construct approximations $\{\tilde{C}_m\}_{m=1}^{M}$ of the first M harmonics over the FOV using linear combinations of the real sensitivity functions. These two steps are performed once for a particular coil configuration. The third step is the imaging process and the reconstruction itself. K images are acquired simultaneously using the original K coils, with a step of $M\Delta k_y$ in the phase encoding direction. Since only every Mth row in k-space is measured, the speedup factor is M. In every phase encoding iteration, M rows in the matrix $S(k_x,k_y)$ are reconstructed using virtual coils of sensitivities $\{\tilde{C}_m\}_{m=1}^{M}$.

Implementation. A standard linear coil array of six elements was used for the experiments reported in the first paper [12]. Later papers mention arrays of eight and ten coils for cardiac imaging. No special hardware is needed for this method.

Interestingly enough, linear coil arrays have been used in MRI for many years to extend the FOV and to increase SNR of the image. This approach was first proposed by Roemer *et al.* [11],

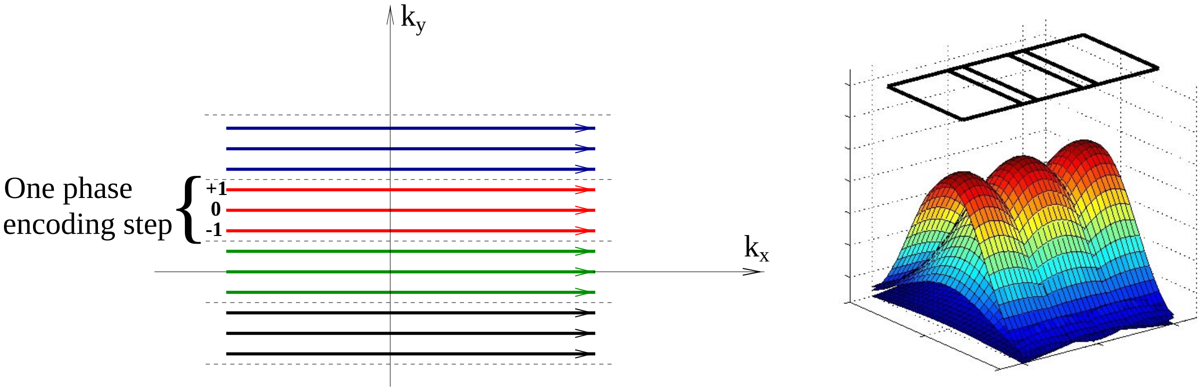

(a) (b)

Figure 7: SMASH MRI. (a) SMASH k-space sampling using three harmonics: rows of the same color are sampled simultaneously. (b) Linear three-element coil array and simulated coil sensitivity functions.

who suggested using multiple coils to obtain more signal per pixel and thus increase SNR. SMASH uses the same coils to reduce acquisition time.

Experimental Results. This was the first fast MRI technique based on parallel imaging demonstrated on real medical images. The first paper included torso images obtained with a speedup factor of two, which reduced the imaging time (and therefore breath-hold time) from 22sec to 11sec. Speedup factors up to six have been reported.

Since then, the technique has been applied to cardiac imaging [14]. Cardiac imaging can benefit greatly from imaging speedup, as many of the motion artifacts are eliminated by a faster imaging technique. An imaging rate of 42slices/sec was demonstrated for cardiac imaging.

It has been demonstrated empirically that SMASH does not reduce SNR significantly compared to the standard techniques. In most cases, SNR of SMASH images is reduced by less than 10% relative to the standard image. And in cardiac imaging, the quality of the images is improved due to removal of motion artifacts.

The main limiting factor for greater speedup is the physical dimensions of the coils. As more coils are placed within the same FOV, the overlap of their sensitivity function increases, and therefore the number of harmonics that can be represented reliably does not grow as fast as the number of coils. The authors mention a speedup factor of 4 using six- and eight-element coils.

Discussion. This is a very promising technique that has already produced significant improvements in cardiac imaging. Two factors are crucial for successful implementation of this method: coil sensitivity estimation and approximation of the first harmonics using the sensitivity functions.

The authors discuss the problem of coil sensitivity estimation in details in the second paper [13]. The main concern is that the coil sensitivity changes between the experiments, as the arrays are usually made to be flexible and fit the imaged body part. In order to overcome this problem, the authors proposed and demonstrated a technique called AUTO-SMASH [8] that samples extra rows in the k-space during image acquisition and estimates the coefficients a_k^m from the extra data obtained in the same configuration as the rest of the image.

The second important factor is the accuracy in approximating the harmonic sensitivity functions of the virtual coils. The authors point out in [8, 13] that errors in this step cause reconstruction errors in the imaging step, because Eq. (51) is not satisfied perfectly. I propose a modification of the method that eliminates reconstruction errors due to an imperfect fit of the harmonics. The main idea is to combine the two steps into one estimation problem using the error in the images, rather than the error in the sensitivity functions, as a measure of the reconstruction quality.

Since only the phase encoding direction is affected by the proposed modifications, the analysis below is done in 1D. This simplifies the derivation, and the second dimension can be added later by using the standard frequency encoding. Thus an image s is represented by a 1D vector of N pixels, and a sensitivity function D can be thought of as a 1D function $D(y)$. Fourier basis is a complete basis that can be used to represent any sensitivity function:

$$D_k(y) = \sum_m b_m^k C_m(y). \tag{53}$$

Theoretically, this sum is infinite, but in practice, the sensitivity function is estimated on a discrete grid, and can therefore be represented as a finite vector. The highest spatial harmonics are determined by the Nyquist theorem (see Section 2.2). Using matrix notation, we represent the coil sensitivity functions as row vectors. In this notation,

$$D = BC, \tag{54}$$

where D is a $K \times L$ matrix of K coil sensitivity vectors (L is the number of samples used to represent the sensitivity functions), B is a $K \times L^0$ matrix of coefficients (L^0 is the number of harmonics used for representing the sensitivity functions, Nyquist defines the relationship between L and L^0), and C is a $L^0 \times L$ matrix whose rows represent the first L^0 harmonics. Since the imaging process is linear, the images obtained by the coils are linear combinations of the images that would have been obtained by the "virtual coils" with sensitivities that are equal to the pure harmonics:

$$\hat{s}_k(i) = \sum_m b_m^k s(i-m) = \sum_m b_m^k [J_1^i J_0 s]_m = b^k (J_1^i J_0) s, \tag{55}$$

where J_0 is a matrix that inverts the order of the elements in a vector, and J_1 is a matrix that shifts elements in a vector by one position. The output image values are equal to the convolution of the row vector b^k with the original image s shifted appropriately. Matrices J_0 and J_1 allow us to represent this operation as matrix multiplication, rather than convolution. If we combine the row vectors of the images into a single matrix $\hat{S}$, its columns satisfy

$$\hat{s}_i = B J_1^i J_0 s. \tag{56}$$

Suppose a speedup factor of M is used. Then the real images are subsampled to N/M pixels, defining $K \times N/M$ equations with N unknowns. If $M \leq K$, this system is over-constrained and can be solved using least squares fit:

$$s_{\text{out}} = \left(\sum_i (B J_1^i J_0)^T (B J_1^i J_0) \right)^+ \sum_i B J_1^i J_0 \hat{s}_i, \tag{57}$$

where X^+ denotes a left pseudo inverse of matrix X:

$$X^+ X = I. \tag{58}$$

Note that we minimize the error in the measured images $\hat{S}$, rather than the error in the sensitivity functions $\tilde{C}$.

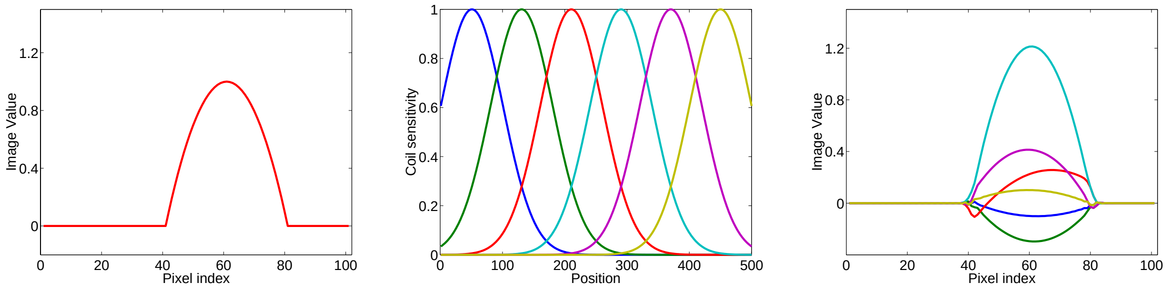

(a) (b) (c)

Figure 8: Artificial example. (a) Original image S in k-space. (b) Six sensitivity functions. (c) Images obtained by these coils. Color coding is identical to (b). In this plot, the images are shown at full resolution (no subsampling).

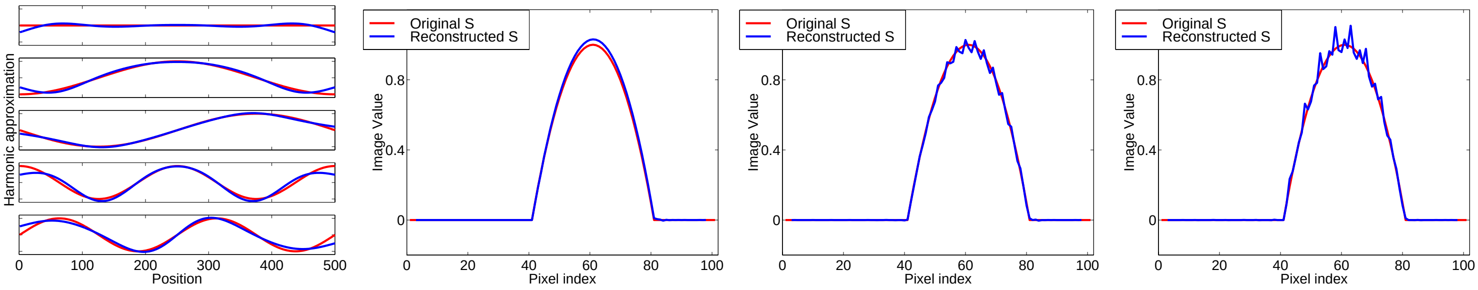

(a) (b) (c) (d)

Figure 9: SMASH reconstruction of the artificial example. (a) Least squares fit approximation of the first 5 harmonic functions. The approximations are shown in blue, the true harmonics are shown in red. (b) SMASH reconstruction, no speedup. (c) Speedup of 3. (d) Speedup of 5.

Setting up the problem this way allows us to analyze the reconstruction errors that occur in SMASH imaging due to imperfect fit of the first M harmonics. Using the representation of Eq. (53), Eq. (52) can be re-written as

$$\tilde{C} = AD = ABC. \tag{59}$$

The solution is the first M rows of $B_{+} = (B^{T^{+}})^{T}$, a right pseudo inverse of B:

$$BB_{+} = I. \tag{60}$$

By performing this step, SMASH limits how much a particular real image can influence the reconstructed image. A pixel in the reconstructed image is affected only by pixels in the real images that are in in the M neighboring locations. Therefore, the influence of any pixel in the real image is limited to the M neighborhood of the pixel position. In the modified approach, any pixel in the real image is allowed to contribute to any pixel in the reconstructed image based on the values of the sensitivity function at those two pixels.

To demonstrate this, I created a simple artificial example. Fig 8 shows the original image s of $N = 100$ pixels in 1D k-space, six coil sensitivity functions and the images obtained by the coils that were computed using $L^0 = 201$ harmonics. Fig 9 shows SMASH reconstruction for different speedup factors. One can see that the reconstruction errors grow as the speedup factor M (subsampling of $\hat{S}$) increases. For comparison, Fig 10a shows the reconstruction obtained from

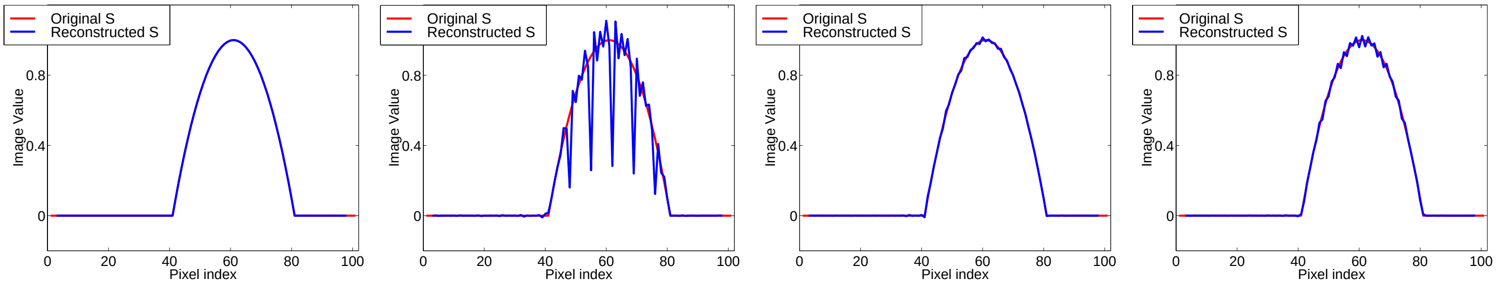

(a) (b) (c) (d)

Figure 10: Reconstruction results using the direct method: (a) Speedup of 6, using 101 harmonics. (b) Speedup of 7, using 101 harmonics. (c) Speedup of 6, using 21 harmonics. (d) Speedup of 6, using 11 harmonics.

Eq. 57. The reconstruction was done for speedup factor $M = 6$, i.e., only every sixth element in each $\hat{s}_k$ was used for reconstruction. For all speedup factors up to 6, the reconstruction is precise. Fig 10b shows the reconstruction for a speedup factor of 7. In this case, some of the original data was missing in the images used for reconstruction. Since we only use 6 coils, we cannot expect to get more information using 6 coils than 6 times the information from one coil. To simulate discrete sensitivity measurements, Fig 10(c,d) show the reconstruction results based on fewer harmonics than what was used for image simulation. The errors appear and grow as the sensitivity estimates get worse. This reinforces the importance of measuring the coil sensitivity with high resolution (and accuracy).

To summarize, the method proposed here can eliminate reconstruction errors due to an imperfect fit of harmonics. This could improve the overall quality of the image reconstruction. The coil sensitivity estimation remains a very important and sensitive part of the algorithm. Better sensitivity estimates will enable further improvements in both the quality of the images and the imaging time, as the reconstruction algorithm will be able to extract more information from the same amount of measurements using better knowledge of the coil sensitivities.

4 Finale

In addition to the general review of MRI principles, two fast MRI techniques have been discussed in the report. They use different approaches to reducing the number of phase encoding steps, and thus reducing the imaging time. While SVD MRI is at an earlier stage and has not been fully implemented yet, SMASH is a mature project that has demonstrated significant improvements for cardiac imaging. I summarized the most important characteristics of both techniques in Table 1. The table includes major implementation features, as well as practical aspects of each method. The original contribution in this report is the error analysis for both methods, which also resulted in a modification of SMASH imaging with reduced reconstruction errors.

Property	SVD MRI	SMASH
k-space sampling	Linear combinations of rows that represent a few largest principal components.	Several adjacent rows simultaneously.
Implementation	Special excitation pulses.	Can be used with any standard imaging method, need to estimate the coil sensitivity functions.
Hardware	Standard rf coils, but need to implement real time pulse profile generation.	Standard linear coil array.
Speedup	Depends on the number of encodes, around 2.	Depends on the number of coils, 2-6.
Speedup limiting factors	Complexity of the images, differences between the estimated image and the real one.	Number of coils that fit along FOV and their sensitivity overlap.
Experimental results	Phantoms and simulations of medical images.	Phantoms and medical scans. Cardiac imaging at 42frames/sec, 2D.
My contribution	Quantitative analysis of the error rate of convergence as a function the number of encodes. Important for picking the optimal number of encodes.	Improvement of the reconstruction quality by using higher order harmonics in computing each coil's contribution to the resulting image.

Table 1: Summary of important characteristics of SVD MRI and SMASH.

References

[1] Cao Y and Levin DN. Feature - recognizing MRI. *Magnetic Resonance in Medicine*, 30:305-317, 1993.

[2] Cao Y and Levin DN. On the Relationship Between Feature-Recognizing MRI and MRI Encoded by Singular Value Decomposition. *Magnetic Resonance in Medicine*, 33:140-142, 1995.

[3] Curry III TS, Dowdey JE and Murry RC, Jr. Christensen's Physics of Diagnostic Radiology. 4th Ed. Lae & Febiger. Philadephia, PA. 1990.

[4] Golub GH and Van Loan CF. Matrix Computations, 2nd Edition. Johns Hopkins University Press. Baltimore, MD. 1989.

[5] Haase A, Frahm J, Matthaei D, Hanicke W, Merboldt KD. FLASH Imaging: Rapid NMR Imaging Using Low Flip-Angle Pulses. *J. Magnetic Resonance*, 67:258-266, 1986.

[6] Hayes CE, Hattes N and Roemer PB. Volume Imaging with MR Phase Arrays. *Magnetic Resonance in Medicine*, 18:309-319, 1991.

[7] Hornak JP. The Basics of MRI. http://www.cis.rit.edu/htbooks/mri

[8] Jakob PM, Griswold MA, Edelman RR, Sodickson DK. AUTO-SMASH: a Self-Calibrating Technique for SMASH Imaging. *Magnetic Resonance Materials in Physica, Biology and Medicine*, 7:42-54, 1998.

[9] Mansfield P and Morris PG. NMR Imaging in Biomedicine. Academic Press. London, England. 1982.

[10] Panych LP, Oesterle C, Zientara GP and Hennig J. Implementation of a Fast Gradient-Echo SVD Encoding Technique for Dynamic Imaging. *Magnetic Resonance in Medicine*, 35:554-562, 1996.

[11] Roemer PB, Edelstein WA, Hayes CE, Souza SP and Mueller OM. The NMR Phased Array. *Magnetic Resonance in Medicine*, 16:192-225, 1990.

[12] Sodickson DK and Manning WJ. Simultaneous Acquisition of Spatial harmonics (SMASH): Fast Imaging with Radiofrequency Coil Arrays. *Magnetic Resonance in Medicine*, 38:591-603, 1997.

[13] Sodickson DK, Griswold MA and Jakob PM. SMASH Imaging. *Magnetic Resonance Imaging Clinics of North America*, 7(2):1-18, 1999.

[14] Sodickson DK. SMASH Web page.
http://134.174.129.110/~dsodicks/Public/smash/smash.html

[15] Leach MO. Spatialy Localised Nuclear Magnetic Resonance. In *The Physics of Medical Imaging*. Ed. S. Webb. Inst. of Physics Publishing. Philadelphia, PA. 1988.

[16] Wright G. An Introduction to MR.
http://www.sunnybrook.utoronto.ca:8080/~gawright/menu_mr_nf.html

[17] Zientara GP, Panych LP, and Jolesz FA. Dynamically Adaptive MRI with Encoding by Singular Value Decomposition. *Magnetic Resonance in Medicine*, 32:268-274, 1994.

[18] Zientara GP, Panych LP, and Jolesz FA. Applicability and Efficiency of Near-Optimal Spatial Encoding for Dynamically Adaptive MRI. *Magnetic Resonance in Medicine*, 39:204-213, 1998.

[19] Zientara GP, Panych LP, and Jolesz FA. Near-Optimal Spatial Encoding for Dynamically Adaptive MRI: Mathematical Principles and Computational Methods. *Int. J. Imaging Systems & Technology*, 10:151-165, 1999.